

# Energy transfer in the spatial evolution of double-wave-group focusing

Binzhen Zhou(周斌珍)<sup>a,b</sup>, Kanglixu Ding(丁康礼玺)<sup>b</sup>, Yi Xiao(肖义)<sup>b</sup>, Lei Wang(王磊)<sup>b,c,\*</sup>,  
Tianning Tang(唐天宁)<sup>d</sup>

<sup>a</sup> State Key Laboratory of Subtropical Building and Urban Science, South China University of Technology,  
Guangzhou 510641, China

<sup>b</sup> School of Civil Engineering and Transportation, South China University of Technology, Guangzhou  
510641, China

<sup>c</sup> Department of Civil and Environment Engineering, The Hong Kong Polytechnic University, Hong  
Kong 999077, China

<sup>d</sup> Department of Engineering Science, University of Oxford, Oxford, OX1 3PJ, United Kingdom

## Abstract

The linear superposition of the individual wave groups underestimates the bimodal waves, as it overlooks the interactions between these wave groups, which is thought to be connected to the generation of extreme waves. Continuing our previous work [1], the energy transfer in the spatial evolution of double-wave-group focusing is highlighted, based on a fully nonlinear numerical wave tank with the High-order Spectral method. The findings reveal that a sea state with a narrower intermodal distance or an uneven distribution of the bimodal spectrum tends to induce larger waves. The third-order nonlinear interaction is primarily triggered by the transient wave focusing, as opposed to a prolonged evolution like the behavior of even-order components. The configurations of the sea state exert varying impacts on the evolution of harmonical energy, with the most potent nonlinearity observed away from the actual focused position, the nonlinear energy amplified relative to the initial state, and the energy redistributed after wave focus. The study also uncovers that during the wave focus and defocus process, waves experience an irreversible energy exchange, with frequencies shifting from higher to lower, likely due to second-order harmonics. These discoveries broaden our comprehension of the nonlinear characteristics inherent in the interaction between the swell and wind-sea waves.

## 1. Introduction

Bimodal sea states, which are common in actual marine environments with an occurrence probability as high as 30% [2], have been proven to be more likely to generate extreme waves. Extreme waves, also known as freak waves, whose wave height is more than twice the significant wave height [3], have been reported as a major responsibility for serious risk to the safety of marine activities [4][5]. Although the nonlinear characteristics at the focused position have been clearly explained, the total energy and the corresponding harmonical energy transfer in the spatial evolution are still unknown. To identify the impact of wave configurations on the occurrence of extreme waves, explore the spatial and temporal evolution patterns of double-wave-groups focusing, and explain the characteristics of harmonical energy transfer, is of significance to understand these nonlinear physics and enrich the theory of nonlinear wave dynamics.

In the bimodal sea state, the corresponding wave exhibits double peaks in the frequency spectrum.

---

\* Corresponding author  
E-mail address: [wangleimme@scut.edu.cn](mailto:wangleimme@scut.edu.cn) (L. Wang)

1 This typically happens when a wind-sea wave (with a relatively higher peak frequency) develops over a  
2 swell wave (with a relatively lower peak frequency), resulting in double wave groups. Previous  
3 research has indicated that in the propagation of double-wave-group focusing, the nonlinear interaction  
4 primarily stems from two aspects [1][6], interactions within a single wave group, and interactions  
5 between different wave groups. Both of these are considered to be key drives in the generation of  
6 extreme waves.

7 Regarding the interactions within a single wave group, the physical mechanism behind extreme  
8 waves has been studied for several decades. It can be categorized into spatial and geometrical focusing  
9 [7], abrupt depth transition [8][9], wave-current interaction [10][11], modulation instability [12], and  
10 two or more of these effects worked simultaneously [13]-[16]. The Spatial-temporal focusing is  
11 considered a key physical mechanism in the formation of extreme events. Rapp and Melville [17]  
12 proposed a phase-focusing method that could be used to reproduce the extreme waves in the  
13 experimental laboratory. Considering the nonlinear interaction, the actual focused amplitudes were  
14 found to exceed the assumed [18], and the actual focused positions were pointed out to deviate from  
15 that predicted by linear theory in both the numerical simulation and experiment [19]. Buldakov et al.  
16 [20] raised an iterative method to correct the deviation based on linear wave components obtained from  
17 the four-phase decomposition [21], which is available to simulate the wave group focusing [11].  
18 Additionally, the expansion of the wave amplitude was explained through some time-frequency  
19 conversion methods, such as the Fast Fourier Transform and Wavelet Transform [22]. The non-resonant  
20 [23] or resonance interaction [24] was proven to be associated with the energy transfer from the low  
21 frequency to the high frequency, contributing to the emergence of large waves [25]. The dispersion  
22 relation consequently varied, with some deviation from the theoretical prediction theory [26].

23 In addition to the interactions within a single wave group which are very common in the propagation  
24 of a single wave group, interactions between wave groups cannot be ignored. Tao et al. [27] found that  
25 the nonlinear interactions between wave groups can promote the magnitude of the water surface  
26 elevation in a long-term evolution of the modulational waves. In other theoretical research [6][28] and  
27 field analysis [29][30], the same conclusion can also be drawn. Rodriguez et al. [31] put forward two  
28 basic parameters to describe the spectral characteristics of a bimodal sea state, the intermodal distance  
29 (ID) and the sea-swell energy ratio (SSER). They pointed out that the wave configurations in the swell-  
30 dominated state ( $SSER < 1.00$ ), the wind-sea-dominated state ( $SSER > 1.00$ ) and the sea-swell energy  
31 equivalent state ( $SSER = 1.00$ ) undergo different nonlinear physics, where the contribution of the second  
32 order interaction was meaningful [32], in particular for a closer intermodal distance [33]. Moreover,  
33 Wang et al. [34][35] analyzed the influence of the configuration of the bimodal waves on the statistical  
34 properties utilizing the High-order Spectral method, demonstrating that ID and SSER have a significant  
35 impact on the nonlinear behaviors of the wave group, particularly for the condition with a closer  
36 intermodal (i.e.,  $ID < 0.10$ ) and an asymmetrical energy distribution ( $SSER \neq 1.00$ ), extreme waves is  
37 more prone to be generated. Additionally, an empirical model to predict extreme waves in the given  
38 bimodal sea state was fitted based on a large number of numerical simulations [34], while the ignoring  
39 of the spatial and temporal evolution limits the applicability of the quantitative formula, even the waves  
40 with a larger steepness. Besides, the evolution of the double-wave-group focusing is preliminarily  
41 explored by utilizing the wavelet spectral method [36], and the process by which the swell wave  
42 catches up to the wind-sea wave is shown. Furthermore, Zhou et al. [1] found more second-order and  
43 third-order harmonics are activated at the focused position utilizing the harmonics analysis.

44 The impact of the sea state on the nonlinear interactions at the focused position has been explained.

However, the evolution of these nonlinear interactions and the transfer of harmonical energy remains unclear. Therefore, we aim to numerically investigate the energy evolution during the process of the double-wave-group focusing. Our work brings three novel contributions. First, focused amplitudes with spectral distribution are compared and the configurations easier to motivate the large waves are identified. Second, the evolution of the harmonical energy is given based on the harmonics analysis. Third, the irreversible energy exchange in the wave focus and defocus is clarified.

The rest of this paper is arranged as follows. In section 2, the numerical modal and configurations of the bimodal sea state are briefly introduced. Section 3 illustrates the evolution characteristics in the time and frequency domain with various spectral distributions. Section 4 analyzes the energy transfer in double-wave-group focusing. Finally, the conclusions are summarized in Section 5.

## 2. Numerical model

### 2.1 Numerical wave tank

Double-wave-group focusing (corresponding to the bimodal sea state) undergoes such complex physical processes, that a fully nonlinear numerical model with an advantage in accuracy and efficiency is needed. There are several types of fully nonlinear numerical wave models currently in existence, such as Computational Fluid Dynamics (CFD) based on the Navier-Stokes equation, Boundary Element Method (BEM) or High-order Spectral (HOS) method based on the Laplace equation, and so on. However, the CFD method not only suffers from numerical dissipation, making it difficult to accurately capture the free surface elevation, but also requires a large number of grids leading to great limitations in computational efficiency. The BEM needs to solve the matrices with great computational complexity and high computational cost. By contrast, the HOS method solves the velocity potential and its derivative terms by Fast Fourier Transform (FFT), with a great advantage in efficiency as well as accuracy. It is preferred when solving extreme waves with strong nonlinearity, and it is successfully applied to simulating single-wave-group focusing [37], double-wave-group focusing [34][36], and even wave co-propagating with opposing current [38].

In this study, a numerical wave model based on the High-order Spectral (HOS) method named HOS-NWT solver [39], is employed to collect the time series data of the water surface elevation in the double-wave-group focusing to be analyzed. Assuming the fluid is incompressible, inviscid, and irrotational, the velocity potential inside the domain,  $\Phi(x, z, t)$  is divided into free surface velocity potential  $\Phi_f$  and additional velocity potential  $\Phi_{add}$ , also satisfying the Laplace equation [40].

$$\nabla^2 \Phi = 0 \quad \text{in } D \quad (1)$$

where  $\nabla = (\partial/\partial x, \partial/\partial z)$ ,  $D$  represents the fluid domain.

Analogous to the advanced HOS model, the free surface kinematic and dynamic boundary conditions are revised as [41] [42]

$$\begin{aligned} \frac{\partial \eta}{\partial t} &= \left(1 + \left|\frac{\partial \eta}{\partial x}\right|^2\right) \frac{\partial \Phi_f}{\partial z} + \frac{\partial \Phi_{add}}{\partial z} - \left(\frac{\partial \Phi_f}{\partial x} + \frac{\partial \Phi_{add}}{\partial x}\right) \frac{\partial \eta}{\partial x} & z = \eta(x, t) \\ \frac{\partial \Phi_f}{\partial t} &= -\eta + \frac{1}{2} \left(1 + \left|\frac{\partial \eta}{\partial x}\right|^2\right) \left(\frac{\partial \Phi_f}{\partial z}\right)^2 - \frac{1}{2} \left|\frac{\partial \Phi_f}{\partial x}\right|^2 - \frac{1}{2} |\nabla \Phi_{add}|^2 & (2) \\ & - \frac{\partial \Phi_f}{\partial x} \cdot \frac{\partial \Phi_{add}}{\partial x} - \frac{\partial \Phi_{add}}{\partial t} & z = \eta(x, t) \end{aligned}$$

in which  $\eta$  denotes the surface elevation of the water wave.

The corresponding bottom and wavemaker boundary conditions are rewritten as

$$\frac{\partial \Phi}{\partial z} = \frac{\partial \Phi_f}{\partial z} + \frac{\partial \Phi_{add}}{\partial z} = 0 \quad z = -h \quad (3)$$

$$\frac{\partial S}{\partial t} = \frac{\partial \Phi_{add}}{\partial x} \quad x = 0 \quad (4)$$

where  $h$  denotes the water depth, and  $S$  is the displacement of the wavemaker.

Based on these boundary conditions, the calculation domain is initialized as:

$$\begin{cases} \eta(x, t = 0) = 0 \\ \Phi_f(x, t = 0) = 0 \end{cases} \quad (5)$$

$\Phi_f$  satisfies the Laplace equation, the free surface boundary conditions, and the bottom boundary condition, and can be expressed in a perturbation series up to arbitrary nonlinear order solved by the Fast Fourier Transform according to the traditional HOS method [41].  $\Phi_{add}$  satisfies the Laplace equation, the wavemaker boundary condition, and the bottom boundary condition, and can be obtained from the linear wavemaker theory [43]. After gaining all the terms on the right side of the rewritten boundary equations, the velocity potential and the free surface elevation in the next time step can be calculated through the time integration using the fourth-order Runge–Kutta method.

The numerical wave tank based on the HOS method is illustrated in Fig. 1. The wavemaker is located on the left side and the absorbing zone is on the other side, with a working depth  $h=1.0$  m, and a horizontal length  $L_x=32$  m. The focused position and the focused time are assumed as  $x_b=15$  m and  $t_b=50$  s. A series of wave gauges are set away from the wavemaker from 5.0 m to 25.48 m to record more time history information along the wave propagation.

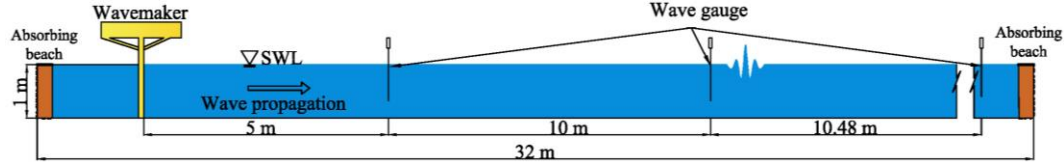


Fig. 1 Sketch of the numerical wave tank.

## 2.2 Bimodal sea state

The iterative method proposed by Buldakov et al. [20] is comprised to correct the deviation of the actual focused position relative to the assumed focused position in single-wave-group focusing. Subsequently, the linear superposition of two corrected wavemaker signals of the corresponding single wave group is adopted to generate the double-wave-group focusing. This method is also applied to the study of Zhou et al. [1]. The validation of the method can be referred to APPENDIX A.

Generally, Sea-Swell Energy Ratio (SSER) and Intermodal distance (ID) are the two major characteristics of the bimodal sea state [31], characterizing the energy ratio of swell system (low-frequency partition) and wind-sea system (high-frequency partition) as well as the peak frequency space between them, respectively.

$$SSER = \frac{m_{02}^2}{m_{01}^2} \quad (6)$$

$$ID = \frac{f_{p2} - f_{p1}}{f_{p1} + f_{p2}} \quad (7)$$

where  $m_0$  is the zero-order spectral moment,  $f_p$  represents the peak frequency, and subscripts 1 and 2 denote the swell and wind-sea systems, respectively.

13 cases with equivalent energy are chosen to be simulated, considering configurations with various values of SSER and ID, listed in Tab. 1. The total number of wave components is fixed as 193 uniformly distributed in the same spectral range  $\Delta f = 0.5 \sim 2.0$  Hz.  $A_b$  represents the assumed focused amplitude, and  $k_p$  represents the peak wavenumber corresponding to the peak frequency and can be obtained from the dispersion relation. Note that the steepness  $k_p A_b$  of the equivalent single wave group is set as 0.15, which is defined as a moderate value not large enough to result in wave breaking. The corresponding input amplitude spectra are presented in Fig. 2.

Tab. 1 Detailed configurations of the bimodal sea states.

| Case | $A_{b1}$ (m) | $f_{p1}$ (Hz) | $k_{p1}A_{b1}$ | $A_{b2}$ (m) | $f_{p2}$ (Hz) | $k_{p2}A_{b2}$ | ID   | SSER |
|------|--------------|---------------|----------------|--------------|---------------|----------------|------|------|
| 1    | 0.025        | 1.008         | 0.102          | 0.025        | 1.008         | 0.102          | 0.00 |      |
| 2    | 0.025        | 0.956         | 0.092          | 0.025        | 1.057         | 0.112          | 0.05 |      |
| 3    | 0.025        | 0.924         | 0.086          | 0.025        | 1.085         | 0.119          | 0.08 |      |
| 4    | 0.025        | 0.903         | 0.082          | 0.025        | 1.103         | 0.122          | 0.10 | 1.00 |
| 5    | 0.025        | 0.791         | 0.063          | 0.025        | 1.186         | 0.142          | 0.20 |      |
| 6    | 0.025        | 0.733         | 0.055          | 0.025        | 1.222         | 0.150          | 0.25 |      |
| 7    | 0.032        | 0.984         | 0.123          | 0.016        | 1.331         | 0.113          |      | 0.25 |
| 8    | 0.027        | 0.899         | 0.089          | 0.022        | 1.216         | 0.133          |      | 0.67 |
| 9    | 0.026        | 0.876         | 0.082          | 0.024        | 1.185         | 0.133          |      | 0.80 |
| 10   | 0.025        | 0.847         | 0.073          | 0.025        | 1.146         | 0.132          | 0.15 | 1.00 |
| 11   | 0.024        | 0.821         | 0.065          | 0.026        | 1.111         | 0.131          |      | 1.25 |
| 12   | 0.022        | 0.803         | 0.059          | 0.027        | 1.087         | 0.130          |      | 1.50 |
| 13   | 0.016        | 0.755         | 0.037          | 0.032        | 1.022         | 0.133          |      | 4.00 |

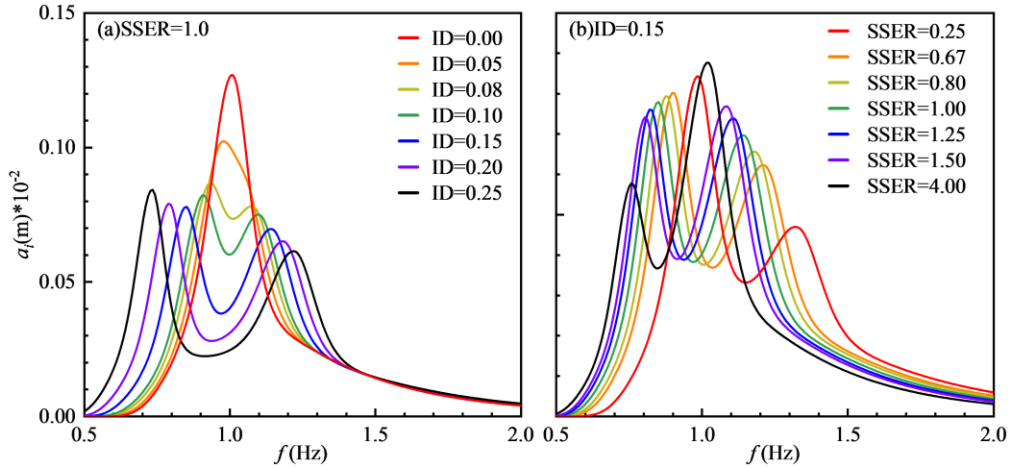


Fig. 2 Input amplitude spectra of the prescribed bimodal sea states, (a) with different values of ID, (b) with different values of SSER.

The established numerical wave tank is validated in APPENDIX B with the wave configuration of Case 4 (ID=0.1, SSER=1.0), available for the coming simulations.

### 3. Evolution characteristics in time and frequency with spectral distributions

#### 3.1 Evolution of double-wave-group focusing

Due to the nonlinear interactions in the wave propagation, the actual focused position and the focused amplitude will deviate from the assumed. In our study, the actual focused position is defined as

the position that the largest crest reaches its maximum. For example, the actual focused position of Case 5 in this section is at  $x_{ab}=15.2$  m. Fig. 3 gives the evolutions of the double-wave-group focusing including wave surface elevation (represented by white lines) and the corresponding wavelet spectrum (represented by colored contours where the color bar represents the nondimensional wavelet energy ratio of energies relative to the maximal energy). Information is collected at 5 locations, namely 2 before, 1 at, and 2 behind the actual focused position, respectively.  $\lambda_z$  is defined as the average zero-crossing wavelength obtained from  $T_z$ .  $A_b$  ( $=A_{b1}+A_{b2}$ ) is the total amplitude of double-wave-group focusing. Near the wavemaker (Fig. 3a), there are two separated wave groups with concentrated energy initially, long waves (with relatively high peak frequency) chasing short waves (with relatively low peak frequency). With the wave groups converging, high-order harmonics are gradually triggered. Till the actual focused position (Fig. 3c), the surface elevation reaches the maximum value, up to  $\eta/A_b=1.17$ , and even the wavelet power emerges more high-frequency components presenting an inverted triangle shape. After the long waves surpass the short waves (Fig. 3e), the two wave groups gradually separate.

Although the overall process of focusing is like that of single wave group focusing, one very attractive phenomenon is that undergoing the wave group focusing, the two wave groups are different from the two before focusing. It indicates that the energies between the two wave groups are redistributed, which is worthwhile to conduct in-depth research in the following.

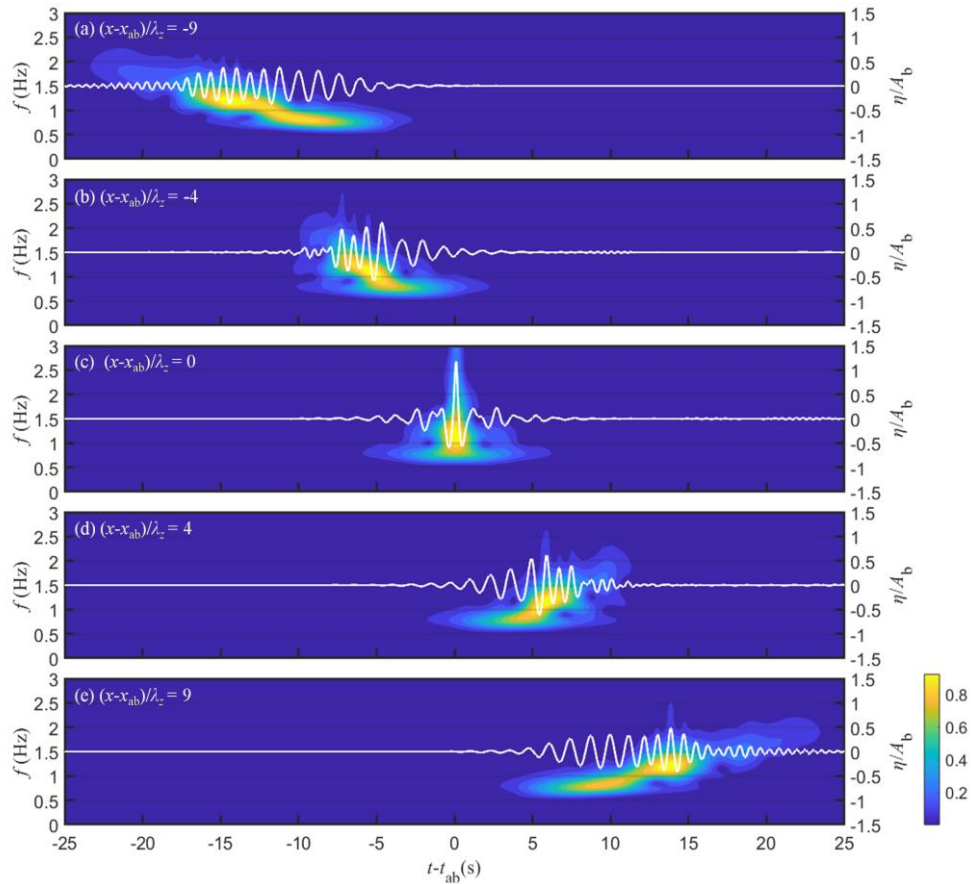


Fig. 3 Evolution of surface elevation and corresponding wavelet spectrum in the process of double-wave-group focusing (Case 5: ID=0.20, SSER=1.00).

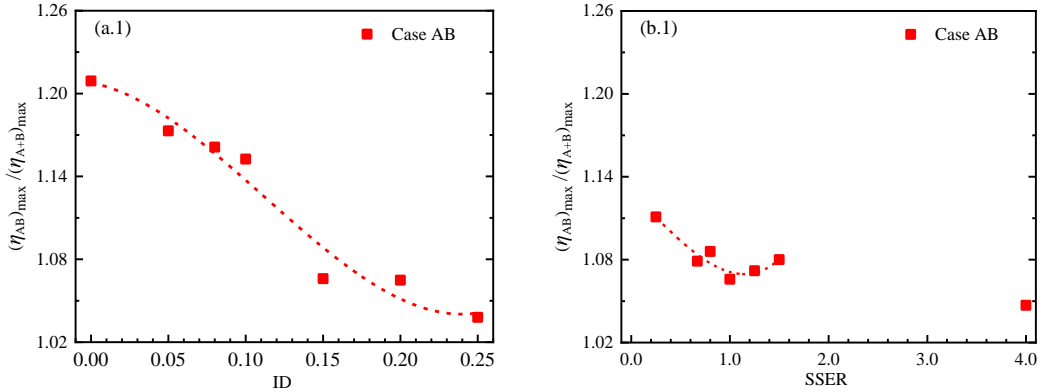
### 3.2 Wave surface elevation at focused position

The difference between Case AB and Case A+B has been pointed out to be associated with the

interaction between wave groups, while that between Case A+B and linear theory is related to the interaction within the single wave group [1]. Fig. 4 analyzes the variation of focused amplitude with various values of ID and SSER, including  $\eta_{AB}$  relative to  $\eta_{A+B}$  (i.e.,  $(\eta_{AB})_{\max}/(\eta_{A+B})_{\max}$ , represented by red squares) and  $\eta_{A+B}$  relative to linear theory (i.e.,  $(\eta_{A+B})_{\max}/A_b$ , represented by blue dots), to compare the impact of spectral distribution on these two interactions.

In Fig. 4a, with the increase in ID, apparent discrepancies in the interactions between wave groups and those within the single wave group happen.  $(\eta_{AB})_{\max}/(\eta_{A+B})_{\max}$  firstly falls rapidly and then trends stable, with values from 1.21 to 1.04, while  $(\eta_{A+B})_{\max}/A_b$  slightly increases. This is because, on one hand, as the peak frequency space increases, the wind-sea system becomes steeper (seen Tab. 1) and its nonlinearity correspondingly enhances. This leads to a slight increase in  $(\eta_{A+B})_{\max}/A_b$ , namely a slight enhancement of the interactions within the single wave group, that is to say, the steeper the wave profile, the stronger the nonlinearity, the more sensitive the numerical model, and the more the significant nonlinear behavior. On the other hand, the larger the value of ID, the wider the spectral bandwidth, and the fewer wave components in the crossing region, inducing weaker interactions between the swell system and the wind-sea system.

Unlike the monochronic tendency with various values of ID, different variations with SSER are illustrated in Fig. 4b. Both  $(\eta_{AB})_{\max}/(\eta_{A+B})_{\max}$  and  $(\eta_{A+B})_{\max}/A_b$  firstly decrease and then increase with the increase of SSER, except one point at SSER = 4.0. The minimum values appear at SSER = 1.0, consistent with the variation of wave amplitude observed in the physical experiment [1] and maximum kurtosis statistics from the numerical results [34]. This proves that asymmetry spectra distributions promote the interaction between wave groups as well as the interaction within the wave group. The influence of ID and SSER on the nonlinear interaction manifests that the closer the intermodal distance (smaller value of ID), the more disequilibrium the spectral distribution (SSER < 1.00 or SSER > 1.00), and the larger the focused amplitude, meaning the more components participated in the energy transfer.





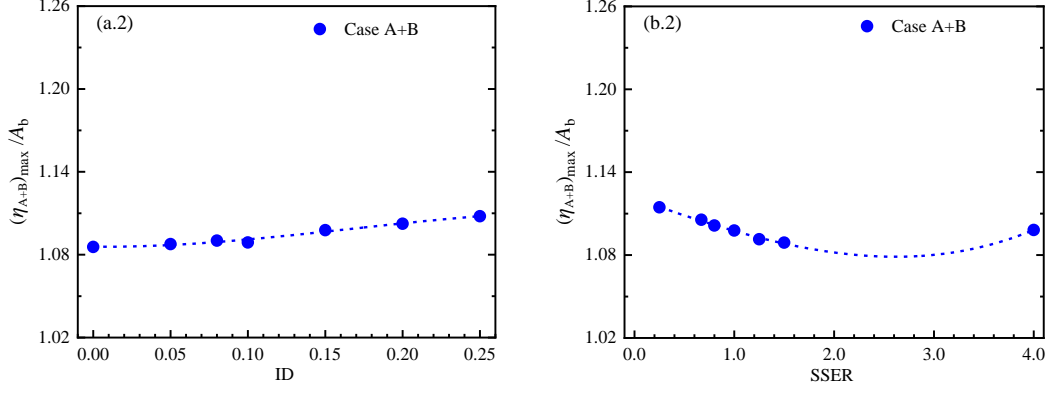


Fig. 4 Variations of focused amplitude in bimodal sea states with various values of ID (a) and SSER (b).

(1)  $(\eta_{AB})_{\max}/(\eta_{A+B})_{\max}$  and (2)  $(\eta_{A+B})_{\max}/A_b$ .

### 3.3 Evolution of frequency spectra

Fig. 5 compares the evolution of frequency spectra between Case AB (represents the sum of interactions within and between wave groups, marked with solid lines) and Case A+B (represents the interactions within wave groups, marked with dotted lines), taking one wave configuration as an example. In the figure, the vertical axis is normalized by the maximum value of the amplitude spectrum (namely  $a_{\max}$ ) of Case A+B.

At the initial stage (at the position 9 times the characteristic wavelength before the focused), the black solid line coincides with the black dotted line in the swell system (corresponding to the relatively low-frequency partition) but lies above the black dotted line in the wind-sea system (corresponding to the relatively high-frequency partition). It demonstrates that the interactions between wave groups begin to emerge at that moment. As the waves propagate to the focused position, their nonlinearity reaches the maximum, accompanied by a greater deviation between the red solid line and the red dotted line in the higher frequency region. These phenomena are consistent with our previous experimental study [1]. The enhancement of the interaction between wave groups activates more substantial nonlinearity, closed related to the increase in focused amplitude of Case AB relative to Case A+B observed in Fig. 4a.1. As the swell waves (relatively long waves) gradually surpass the wind-sea waves (relatively short waves), the energies in the fundamental frequency range tends to go back to the initial state, and those of the higher-order harmonics weaken. Yet, the energy in this state is not completely synchronized with the initial, although the propagation distance between these two stages is the same. Compared to Case A+B, it seems that more wave components are transferred to the wind-sea system for a local broadened bandwidth exhibited in Case AB, probably due to the presence of interactions between two wave groups. It suggests that nonlinear interactions in the process of double-wave-group focusing induce the redistribution of spectral energy in the process of focus and defocus with the same evolutionary distance.



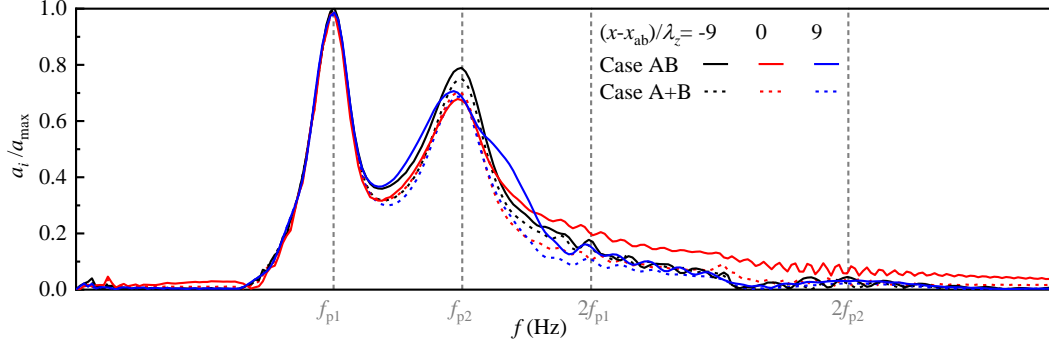


Fig. 5 Evolution of frequency spectra (Case 5: ID=0.20, SSER=1.00).

#### 4. Energy transfer in double-wave-group focusing

##### 4.1 Evolution of total energy in time and space

To explain the evolution of energy in the process of double-wave-group focusing, the total energy of the numerically simulated waves should be given first, shown in Fig. 6 including temporal evolution (Fig. 6a) and spatial evolution (Fig. 6b), in which  $T_z$  is defined as the average zero-crossing period to describe the distribution of a bimodal sea state [44].

From Fig. 6a, it can be observed that after all components of the wave group are generated from the wavemaker and before being dissipated by the absorbing layer, the total energy remains constant for a long time, proving that the energy of the entire closed system is conserved. This means that with the propagation of a bimodal wave group, only kinetic energy and potential energy undergo mutual conversion. The corresponding variation of potential energy is given in Fig. 6b. As approach the actual focused position, the potential energy gradually grows and exhibits bimodal behavior. Note that the maxima of the potential energy fails to be at the actual focused position, which does not conform to our conventional cognition. It is quite necessary to explore what exactly happens during the double-wave-group focusing consequently.

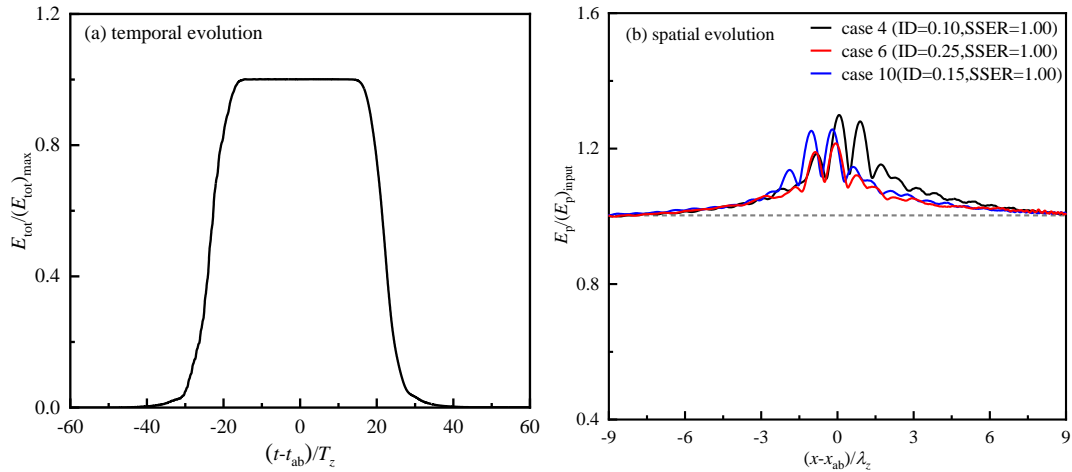


Fig. 6 Evolution of total energy in the process of double-wave-group focusing. (a) temporal evolution, and (b) spatial evolution.

##### 4.2 Evolution of harmonical energy

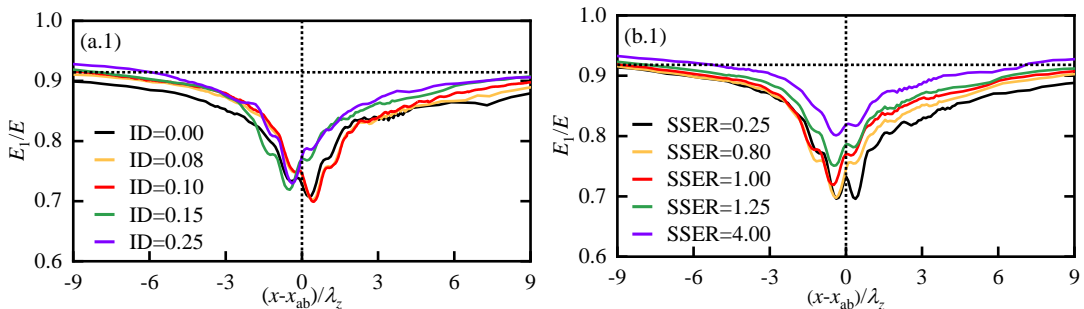
The harmonics analysis of the focused wave group can be conducted by utilizing the four-phase

decomposition method [21]. Inspired by this, the total energy can be divided into four parts, representing linear part ( $E_1$ ), second-order sum part ( $E_2$ ), third-order part ( $E_3$ ), and second-order difference and fourth-order part ( $E_4$ ), which has been successfully available in tracking the energy transfer in the focused process [45][46]. Fig. 7 illustrates the spatial evolution of harmonic energy with various values of ID and SSER, in which the vertical axis represents the harmonic energy ( $E_i$ ) normalized by the corresponding total potential energy (i.e., the energy sum of various order harmonics, that is,  $E = E_1 + E_2 + E_3 + E_4$ ) and the horizontal axis ( $(x-x_{ab})/\lambda_z$ ) represents the number of the waves away from the actual focused position. The vertical dotted line represents the actual focused position, and the horizontal dotted line represents the initial harmonic energy of Case 4 (ID=0.10 and SSER=1.00) in Fig. 7a and Case 10 (ID=0.15 and SSER=1.00) in Fig. 7b.

In Fig. 7, the overall spatial evolution of harmonical energy is quite similar irrespective of the energy ratio or the intermodal distance. In the initial stage of the wave propagation, the value of  $E_1/E$  weakly declines, accompanied by a little increase of  $E_2/E$ . When waves approach a position about three times the characteristic wavelength, higher-order nonlinear interactions can be motivated by sufficient evolution, with a sudden enhancement of  $E_2/E$ ,  $E_3/E$ , and  $E_4/E$  and a sharp drop of  $E_1/E$ . Till near the focused position, the proportion of nonlinear energy is up to 30%. As the wave propagates away from the focused position, the proportion of the harmonic energy gradually approaches the initial state.

However, the state of the peak looks different influenced by the energy ratio and intermodal distance. The behaviors of  $E_1/E$  exhibit bimodal, with a peak before and after the focused position. In Fig. 7a1, for configurations with smaller ID values ( $ID \leq 0.10$ ), as the value of ID becomes larger, the energy decreases in the fundamental frequency range, and the position where the peak energy appears lags further behind the focused position. For those with larger ID values ( $ID > 0.10$ ), the maximum of fundamental energy occurs before the actual focused position, and the larger the value of ID, the larger the proportion of linear energy, and the smaller the deviation from the focused position. These mean that when the wind-sea partition and the swell partition have not yet been completely separated [34][36], there are interactions between wave groups resulting in a longer evolutionary distance and more high-frequency components. In Fig. 7b1, as the value of SSER becomes larger, the peak before the focused position as well as that behind the focused position gradually decreases and the decrease behind the focused position is more pronounced, reflecting that the more disequilibrium the energy distribution, the weaker the nonlinear interaction. The above phenomena can be also used to help explain the variation of nonlinear statistics observed in bimodal sea states with various energy ratios or with various intermodal distances [30][35].

Additionally, although the proportion of the harmonic energy gradually approaches the initial state as the wave propagates away from the focused position, the energy does not completely return to the initialization. This indicates that the nonlinear interaction that occurs during the wave propagation is irreversible, which is the typical difference between lights and waves.



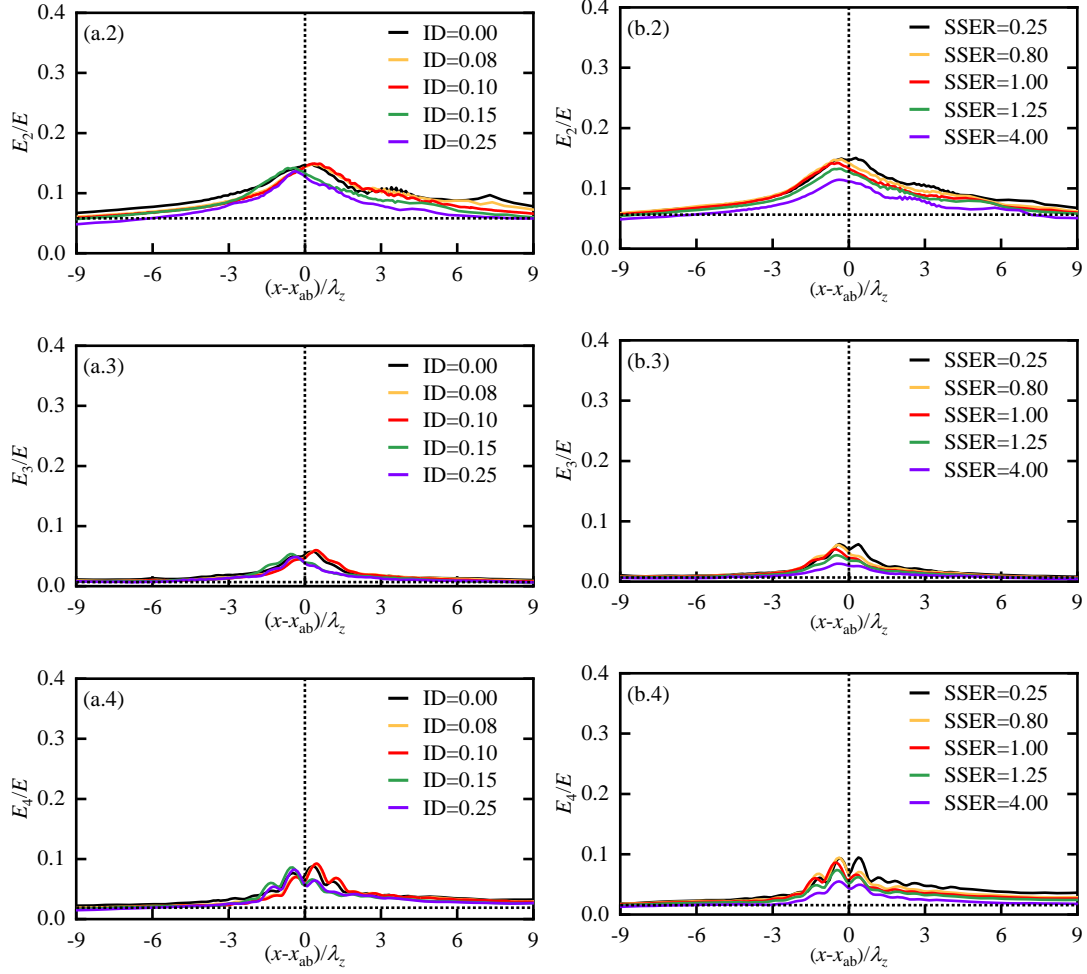


Fig. 7 Spatial evolution of harmonical energy in double-wave-group focusing with various values of ID (left: a) and SSER (right: b). (1)  $E_1/E$ , (2)  $E_2/E$ , (3)  $E_3/E$ , and (4)  $E_4/E$ .

#### 4.3 Properties of energy transfer

The Complex interactions during wave propagation facilitate energy transfer, being an intrinsic trigger of wave profile. In the process of double-wave-group focusing, the maximum values of the harmonical energy do not occur at the actual focused position due to the high-order nonlinearity. To investigate the patterns of the variation, three parameters are used to describe the properties of energy transfer.

(1)  $\Delta$  is defined as the deviation of the position with the strongest nonlinearity relative to the actual focused position, expressed as

$$\Delta = (x_e - x_{ab}) / \lambda_z \quad (8)$$

where  $x_e$  is the position corresponding to the peak point in the evolution of different harmonical energies.

(2)  $E_v$  is defined as the relative difference between the peak value and the initial value, to measure the maximum amplification in the process of harmonical energy evolution, written as

$$E_v = (E_e - E_L) / E_L \quad (9)$$

where  $E_L$  and  $E_e$  represent the value of the harmonical energy at the prescribed initial position (i.e.,  $(x -$

$x_{ab})/\lambda_c=9)$  and at the corresponding peak point, respectively.

(3)  $E_d$  is defined as the energy difference of the same evolutionary distance before and after the wave group focusing, to evaluate the symmetry of the energy transfer in the focusing process, given as

$$E_d = E_R - E_L \quad (10)$$

where  $E_R$  represents the value of the harmonical energy at  $(x-x_{ab})/\lambda_c=9$ .

#### 4.3.1 Deviation of the position with the strongest nonlinearity

Fig. 8 gives the deviation of the position with the strongest nonlinearity relative to the actual focused position in various configurations of double-wave-group focusing. In Fig. 8a, when the values of ID are smaller than 0.10, the deviation of the position  $\Delta$  present positive, demonstrating that the peak value of each harmonical energy appears behind the actual focused position, and otherwise for larger values of ID. Meanwhile, the variation of  $E_1$  and  $E_2$  with ID are quite similar, both initially stabilizing or steadily increasing, and then gradually decreasing to stable when it reaches 0.10. While concerning  $E_3$  and  $E_4$ , they are significantly reduced at the moment the ID becomes larger, showing greater sensitivity to the changes in the intermodal distance. In Fig. 8b, when SSER equals 1.0, the deviations of the position with the strongest nonlinearity before the focused position reaches the maximum except for that of the second-order sum (slightly earlier), reflecting that the weakest nonlinearity happened in the wind-sea and swell equivalent sea state is attributed to the combination of all wave components, although the effect of the second-order sum is minor. This is a little different from the observation by Wang et al. [34], that the point SSER=1.0 is the inflection point of nonlinear statistical parameters, with a minimum value. It is because the corresponding value of ID is different, the previous one with ID=0.10 and here ID=0.15, taking on different energy distribution. In a word, when the value of ID is lower than 0.10 or SSER lower than 0.67, the position where the strongest nonlinearity occurs is delayed relative to the actual focused one, but otherwise for the value of ID more than 0.10 or SSER more than 0.67.

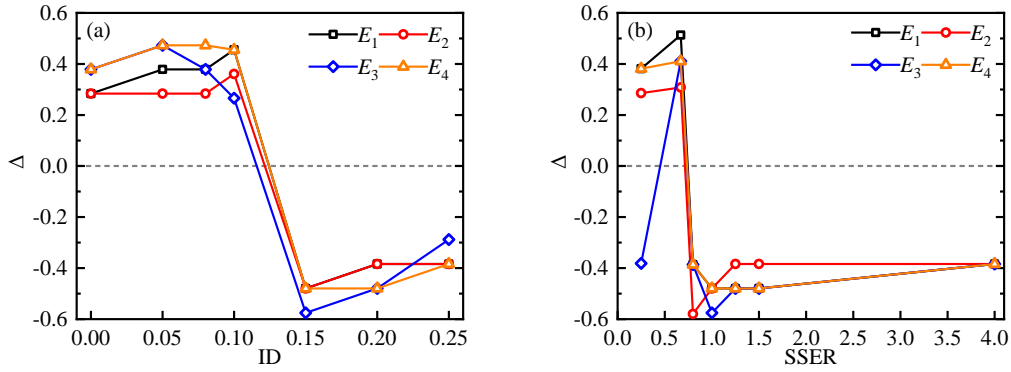


Fig. 8 Deviation of the position with the strongest nonlinearity relative to the actual focused position in various configurations of double-wave-group focusing, (a) with various values of ID, and (b) with various values of SSER.

#### 4.3.2 Maximum amplification during the evolution of harmonical energy

The maximum amplification  $E_v$  in the process of harmonical energy evolution in various wave configurations is presented in Fig. 9.

In Fig. 9a, with the increase of the intermodal distance, the energies of the nonlinearity (including  $E_2$ ,  $E_3$ , and  $E_4$ ) significantly grow up and the blue line (i.e.,  $E_3$ ) is always at the top along with the orange

line (i.e.,  $E_4$ ) second. Till  $ID=0.10$ , the amplification  $E_v$  corresponding to  $E_3$  reaches its maximum, nearly 6.36 times the initial value, while that corresponding to  $E_2$  and  $E_4$  achieves a stable state, with an equilibrium value but less than  $E_3$ . It reflects that when the swell partition and the wind-sea partition are separated (i.e.,  $ID>0.10$ ), the third-order nonlinearity weakens, with minimal impact on the second-order and the fourth-order nonlinearity, indicating that the increased energy of the third-order nonlinearity mainly comes from the interaction between wave groups. Meanwhile, compared to the linear components, the fourth-order components are pointed out to be reduced by three orders of magnitude, while the second-order components are reduced by only one order of magnitude [47][48], which also can be observed in our nonlinear analysis of wavenumber-frequency spectra given in Fig. 13 (APPENDIX C). Suppose that the fourth-order components are too little to be taken note of the energy of the second-order difference is stronger than that of the second-order sum.

Concerning the variation with SSER (Fig. 9b), the overall trend is that increases rapidly and then decreases slowly, and the increased magnitude of the third-order components relative to that of the second-order difference components is also more significant. Near the point at  $SSER=0.67$  which seems a swell-dominated state, the maximum values of the energy from the high-order components emerge. Till  $SSER=1.50$ , a steady state is obtained for the energy amplification of nonlinear harmonics. This phenomenon may be a little different from our previous study [30], in which the wave configuration with wind-sea-swell equivalent has the weakest nonlinearity, explained by the fact that the value of the intermodal distance is not the same.

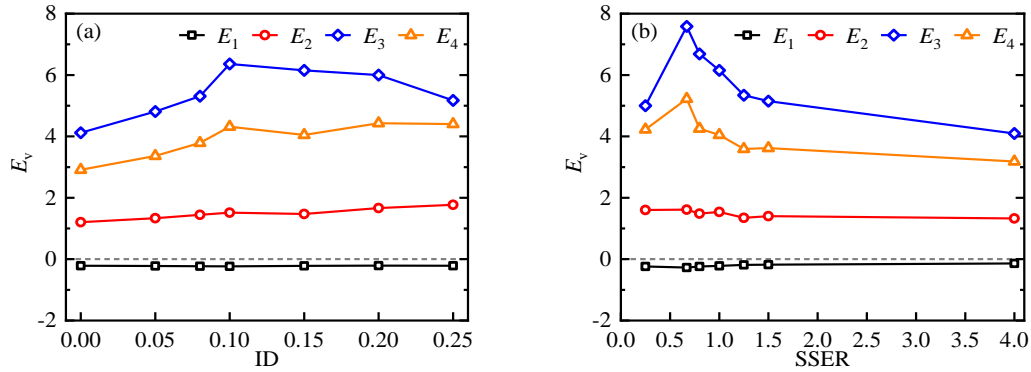


Fig. 9 Proportion of the maximum amplification during the evolution of harmonical energy in various configurations of double-wave-group focusing, (a) with various values of  $ID$ , and (b) with various values of  $SSER$ .

#### 4.3.3 Energy difference before and after focusing

As defined in Eq. (10),  $E_d$  measures the difference between the harmonical energy at the position behind and before the focused position. The corresponding variations in different sea states are presented in Fig. 10. A quite attractive phenomenon is that the energy difference of  $E_1$  and  $E_3$  are always negative and that of  $E_2$  and  $E_4$  are positive. This means that after the evolution of double-wave-group focusing, the energy of odd-order components is being transferred to even-order components.

Although the third-order energy is intensively active as the swell waves collide with the wind-sea waves (Fig. 9a), there are quite tiny energy differences of  $E_3$  (Fig. 10a), suggesting that the third-order nonlinear interaction is mainly triggered by the transient effect of the wave focusing rather than a long-term evolution. For various values of  $ID$ , the energy difference of even order components (i.e., the red line and the orange line) always remains at a higher level, that is, the energy of even order components

is almost going with the entire evolution process. Moreover, as the intermodal distance enlarges, the interactions between the swell and wind-sea decay, and the nonlinear energy difference take on a decreasing trend. When  $ID > 0.15$ , owing to the enhancement of the wave steepness in wind-sea waves, the energy difference rises again.

In Fig. 10b, the energy differences between  $E_2$  and  $E_4$  dramatically reduce as the energy of the wind-sea system increases (i.e., the value of SSER increases), still over that of  $E_3$ . This implies again that the even-order interaction, especially the second-order difference impact, dominates the energy difference before and behind the focusing. The maximum amplification during the harmonic evolution and the energy difference before and after focusing reach their maximum value in the swell-dominated state ( $SSER < 1.00$ ), respectively. Then, the nonlinear interaction and energy transfer are impaired with the energy of the wind-sea increasing ( $SSER \geq 1.00$ ). Interestingly, in the sea states with swell and wind-sea equivalent (i.e.,  $SSER = 1.00$ ) and dominated by wind-sea (i.e.,  $SSER > 1.00$ ), the energy difference of  $E_1$  is equal to that of  $E_4$ , and so is the difference of  $E_3$  and  $E_2$ . That is to say, at this moment, the linear components tend to transfer to the second-order difference, and the third-order to the second-order sum, revealing a pattern of energy transfer that energy inclines to move to a lower frequency band.

The phenomenon with unequal energy distribution at the symmetric position before and behind the focused position, confirms that some new frequency components are generated in the process of the wave focusing and wave defocusing, resulting in the variation of the dispersion relation given in Fig. 13 (APPENDIX C).

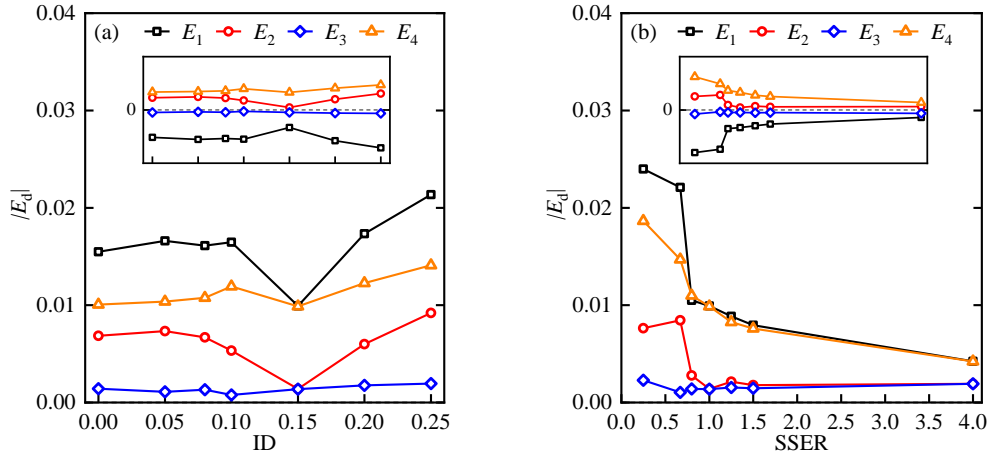


Fig. 10 Proportion of the harmonical energy difference before and after the wave group focusing in various sea states, (a) with various values of ID, and (b) with various values of SSER.

## 5. Conclusions

In this paper, the spatial evolution of the double-wave-group focusing is numerically simulated based on a fully nonlinear wave tank. Variations of time and frequency characteristics and the energy transfer properties are analyzed. The main conclusions are as follows:

- (1) The closer the intermodal distance (ID), the more disequilibrium the spectral distribution, and the larger the focused amplitude. The focused amplitude of double-wave-group focusing relative to that of the linear superposition of the corresponding single-wave-group focusing, namely  $(\eta_{AB})/(\eta_{A+B})$ , decreases monotonously with the increase of ID, but first reduces and then increases with the increase of the sea-swell energy ratio, with the minimum in the sea-swell energy equivalent state (i.e.,  $SSER = 1.00$ ).

(2) The evolution of the nonlinear energies is not a symmetrical process. They begin to be activated at a position three times the characteristic wavelength before the focus. Then they achieve their maximum value near the focus, but not yet exactly at it. After that, they tend to revert to their symmetrical state but actually do not. Additionally, the third-order nonlinear interaction is primarily triggered by the transient effect of the wave focusing, rather than a long-term evolution like that of the even-order components.

(3) In a state with a closer intermodal distance (i.e.,  $ID < 0.10$ ) or one that is swell-dominated (i.e.,  $SSER < 1.00$ ), the strongest nonlinear energy occurs behind the actual focused position. Conversely, in other states, it occurs forward. The greatest deviation relative to the actual focused position occurs in the swell-sea energy equivalent state (i.e.,  $SSER = 1.00$ ).

(4) A configuration with ID of 0.10 or a swell-dominated state with SSER of 0.67 is more likely to amplify the nonlinear energy, with a magnification factor of 6.36 or 7.58 for  $E_3$ , respectively. For other configurations with an ID greater than 0.15, the energy amplification of even-order harmonics tends to stabilize, while that of third-order harmonics gradually decreases.

(5) The energy asymmetry before and after the wave focus indicates an irreversible energy transfer from a relatively higher frequency to a nearby lower frequency. The sea state with a wider intermodal distance (i.e.,  $ID > 0.10$ ) or swell-dominated (i.e.,  $SSER < 1.00$ ) increases the initial energy in the system with a relatively lower frequency. This suggests that the bound waves activated by the amplitude modulation promote a pattern where linear components transfer to the second-order difference, and the third-order to the second-order sum.

These findings enhance our understanding of the configuration under which large waves are more likely to occur, thereby contributing to the knowledge of extreme wave generation. The ability to quickly identify configurations that are more likely to trigger larger waves can guide practical engineering decisions, such as the placement of marine structures and the planning of shipping routes.

In conclusion, the energy transfer in the spatial evolution of a double-wave-group focusing in a uni-directional sea configuration is clarified. In real sea states, waves are distributed not only in the frequency domain but also in the spreading direction. Future research based on this work will investigate two wave groups with different propagation directions in a three-dimensional wave basin. This will likely uncover a multitude of unknown but fascinating physical phenomena.

## Acknowledgments

This work is supported by the National Natural Science Foundation of China (52301319), the National Natural Science Foundation of China National Outstanding Youth Science Fund Project (52222109), the National Natural Science Foundation of China (52071096), Guangdong Basic and Applied Basic Research Foundation (2022B1515020036), Guangzhou Basic and Applied Basic Research Foundation (2023A04J1596), Project of State Key Laboratory of Subtropical Building and Urban Science (2023ZB14), and EPSRC (EP/V050079/1).

## AUTHOR DECLARATION

### Conflict of Interest

The authors have no conflicts to disclose.

### Author Contributions

**Binzhen Zhou:** Conceptualization (equal); Funding acquisition (equal); Project administration (equal); Supervision (lead); Writing – review & editing (equal). **Kanglixi Ding:** Conceptualization



(equal); Methodology (equal); Data curation (lead); Investigation (lead); Visualization (equal); Writing – original draft (lead). **Yi Xiao:** Formal analysis (equal); Investigation (equal); Writing – review & editing (equal). **Lei Wang:** Methodology (lead); Conceptualization (lead); Formal analysis (equal); Funding acquisition (equal); Writing – review & editing (lead). **Tianning Tang:** Investigation (equal); Writing – review & editing (equal).

## DATA AVAILABILITY

The data that support the findings of this study are available from the corresponding author upon reasonable request.

## APPENDIX A: Validation of the iterative method to generate waves

To assess the quality of the corrected waves based on the iterative method, a peak performance (PPS) is introduced, expressed as [49]:

$$PPS = \left( 1 - \frac{(\eta_{\text{linear}_{\text{max}}} - \eta_{\text{target}_{\text{max}}})^2}{\eta_{\text{target}_{\text{max}}}^2} \right) \times 100\% \quad (11)$$

where  $\eta_{\text{target}_{\text{max}}}$  is the assumed focused amplitude (i.e., target focused amplitude), and  $\eta_{\text{linear}_{\text{max}}}$  represents the measured water surface elevation corresponding to the focused position of the linear components which are obtained through the four-phase decomposition method [21].

PPS of each configuration listed in Tab. 1 is given in Fig. 11, where the blue circles and the red triangles denote the cases with relatively higher peak frequency and those with relatively lower peak frequency, respectively. The results show that the overall PPS can achieve a value of more than 99.5%, implying that the shift of focused position can be accurately eliminated by this empirical methodology.

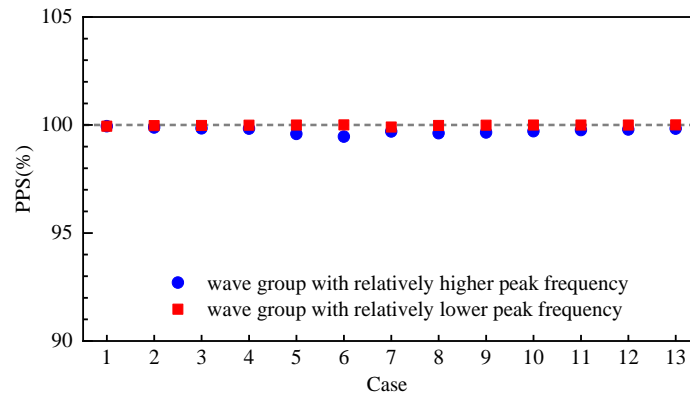


Fig. 11 Peak performance of the iterative methods applied in various wave conditions in our study.

## APPENDIX B: Validation of the numerical modal based on HOS-NWT

To verify the accuracy of the established numerical model, physical experiments are conducted in the wave flume at the Ship and Ocean Engineering Laboratory, South China University of Technology, China. The wave flume is 32 m long, 1 m wide, and 1.5 m deep. The working water depth is kept at 1.0 m. 3 wave gauges are located before, at, and behind the focused position. The configuration can be referred to Case 4 (ID=0.10, SSER=1.00) as listed in Tab. 1. Concerning our numerical simulation using HOS-NWT, the comparison of wave surface elevation between numerical results and experimental data given in Fig. 12 shows a quite good agreement, demonstrating that the numerical model can accurately simulate the evolution of double-wave-group focusing.

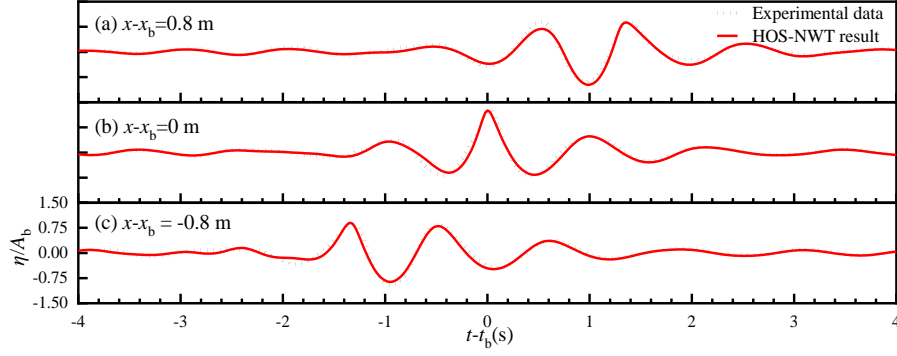


Fig. 12 Comparison of free surface elevations between numerical results and experimental along the wave propagation (Case 4 ID=0.1, SSER=1.0).

### APPENDIX C: Evolution of wavenumber-frequency spectra

The wavenumber-frequency ( $k$ - $f$ ) spectrum specializes in the analysis of the time-frequency characteristics, including the evolution of the amplitude spectra and changes in the dispersive properties of the wave groups [50]. It can be obtained by 2D short-time Fourier transform [22], written as

$$\text{ST}(\tau, f) = \int_{-\infty}^{\infty} x(t) \frac{f}{\sqrt{2\pi}} e^{-((\tau-t)^2 f^2 / 2)} e^{-i2\pi ft} dt \quad (12)$$

Additionally, for a free wave group, the frequency  $f_i$  and the wavenumber  $k_i$  satisfy

$$(2\pi f_i)^2 = g k_i \tanh(k_i h) \quad (13)$$

where  $h$  is the water depth.

For the  $n$ -th order free sup-harmonics, the dispersive relation can be written as [51]

$$(2n\pi f_i)_H^2 = n g k_i \tanh(n k_i h) \quad (14)$$

For the  $n$ -th order bound sub-harmonics, their wavenumbers obey the relation expressed as [51]

$$(2n\pi f_i)_L^2 = g k_i \tanh(k_i h) \quad (15)$$

Fig. 13 illustrates the evolution of the wavenumber-frequency spectrum corresponding to each harmonic, in which  $a_{\max}$  is the maximum amplitude in the frequency domain. The red, blue, and green dash lines denote the dispersion relation of the second-order bound sub-harmonics (obtained from Eq. (15)), linear components (obtained from Eq. (13)), and second-order free super-harmonics (obtained from Eq. (14)), respectively, with the corresponding frequency spectra given on the left. During the propagation of the wave groups, the variations in energy of different harmonics are quite different. Only at the focused position (i.e., there is a most intense interaction between swell waves and the wind-sea waves), fewer fourth-order components appeared in the upper right corner in Fig. 13b4, indicating that throughout the entire evolutionary process, the energy of the fourth-order harmonics is so low that it can be ignored. That is to say,  $E_4$  can be considered as being composed of energy mainly from the second-order difference harmonics. Additionally, compared with the initial state of the wave evolution in Fig. 13a, the deviation from the theoretical nonlinear dispersion relation enlarges in Fig. 13c, resulting in differences such as the enhancement of the high-frequency tail of the linear components and the expansion of the distribution range of the even order components.

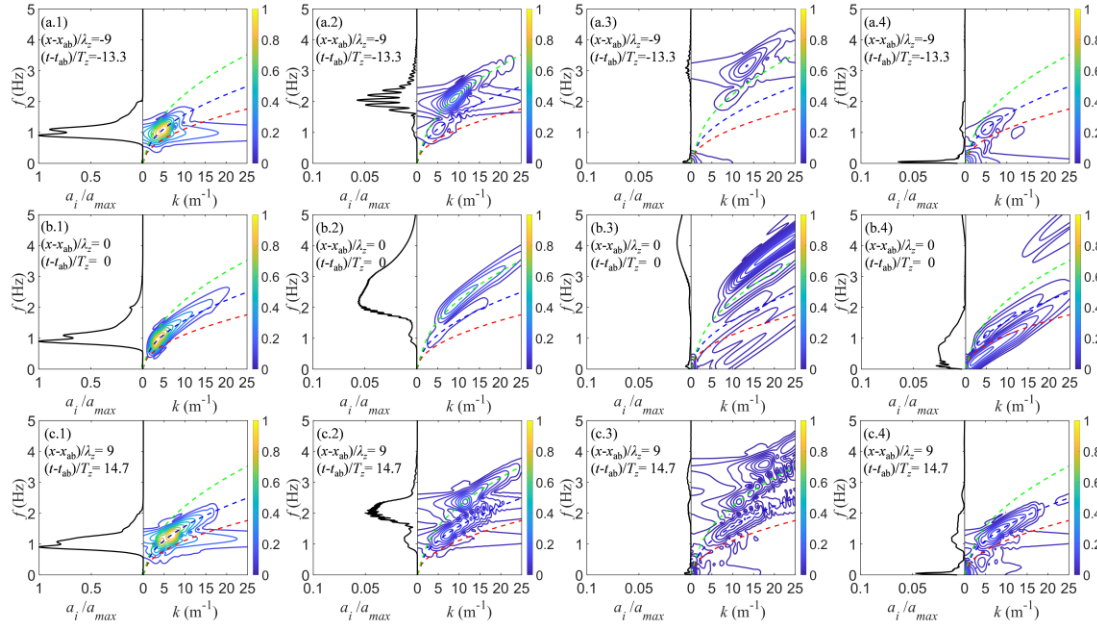


Fig. 13 Wavenumber-frequency spectra of harmonical signals (Case 4 ID=0.10, SSER=1.00).  
(a) before the focused position, (b) at the focused position, and (c) behind the focused position.  
(1) linear energy ( $E_1$ ), (2) 2<sup>nd</sup> order sum energy ( $E_2$ ), (3) 3<sup>rd</sup> order energy ( $E_3$ ) and (4) 2<sup>nd</sup> order  
difference and 4<sup>th</sup> order energy ( $E_4$ ).

## References

1. Zhou B, Ding K, Wang J, et al. Experimental study on the interactions between wave groups in double-wave-group focusing. *Physics of Fluids*, 2023, 35(3): 037118.
2. Vettor R, Soares C. A global view on bimodal wave spectra and crossing seas from ERA-interim. *Ocean Engineering*, 2020, 210: 107439.
3. Dysthe K, Krogstad H, Müller P. Oceanic rogue waves. *Annu. Rev. Fluid Mech.*, 2008, 40: 287-310.
4. Didenkulova E, Didenkulova I, Medvedev I. Freak wave events in 2005–2021: statistics and analysis of favourable wave and wind conditions. *Natural Hazards and Earth System Sciences*, 2023, 23(4): 1653-1663.
5. Häfner D, Gemmrich J, Jochum M. Real-world rogue wave probabilities. *Scientific Reports*, 2021, 11(1): 1-11.
6. Onorato M, Osborne A, Serio M. Modulational instability in crossing sea states: A possible mechanism for the formation of freak waves. *Physical review letters*, 2006, 96(1): 014503.
7. Kharif C, Pelinovsky E. Physical mechanisms of the rogue wave phenomenon. *European Journal of Mechanics-B/Fluids*, 2003, 22(6): 603-634.
8. Draycott S, Li Y, Stansby P, et al. Harmonic-induced wave breaking due to abrupt depth transitions: An experimental and numerical study. *Coastal Engineering*, 2022, 171: 104041.
9. Trulsen K, Zeng H, Gramstad O. Laboratory evidence of freak waves provoked by non-uniform bathymetry. *Physics of Fluids*, 2012, 24(9): 097101.
10. Ma Y, Dong G, Perlin M, et al. Laboratory observations of wave evolution, modulation and blocking due to spatially varying opposing currents. *Journal of Fluid Mechanics*, 2010, 661: 108-129.
11. Chen L, Stagonas D, Santo H, et al. Numerical modelling of interactions of waves and sheared currents with a surface piercing vertical cylinder. *Coastal Engineering*, 2019, 145: 65-83.

12. Benjamin T, Feir J. The disintegration of wave trains on deep water Part 1. Theory. *Journal of Fluid Mechanics*, 1967, 27(3): 417-430.
13. Sarkar A, Chanda A. Structural performance of a submerged bottom-mounted compound porous cylinder on the water wave interaction in the presence of a porous sea-bed. *Physics of Fluids*, 2022, 34(9).
14. Barman K, Chanda A, Tsai C, et al. Bragg scattering of gravity waves by a sea bed of varying depth in the presence of uniform current covered by a floating membrane. *Physics of Fluids*, 2024, 36(1).
15. Li X C, Li, X M, Liao S J . Pattern transition of two-dimensional Faraday waves at an extremely shallow depth. *Science China Physics, Mechanics & Astronomy*, 2016, 59.11: 1-3.
16. Li X C, Li J, Li X M, Liao S J, Chen C H. Effect of width on the properties of Faraday waves in Hele-Shaw cells. *Science China Physics, Mechanics & Astronomy*, 2019, 62.7: 1-6.
17. Rapp R, Melville W. Laboratory measurements of deep-water breaking waves. *Philosophical Transactions of the Royal Society of London. Series A, Mathematical and Physical Sciences*, 1990, 331(1622): 735-800.
18. Baldock T, Swan C, Taylor P. A laboratory study of nonlinear surface waves on water. *Philosophical Transactions of the Royal Society of London. Series A: Mathematical, Physical and Engineering Sciences*, 1996, 354(1707): 649-676.
19. Adcock T, Taylor P. Non-linear evolution of uni-directional focused wave-groups on a deep water: A comparison of models. *Applied Ocean Research*, 2016, 59: 147-152.
20. Buldakov E, Stagonas D, Simons R. Extreme wave groups in a wave flume: Controlled generation and breaking onset. *Coastal Engineering*, 2017, 128: 75-83.
21. Fitzgerald C, Taylor P, Taylor R, et al. Phase manipulation and the harmonic components of ringing forces on a surface-piercing column. *Proceedings of the Royal Society A: Mathematical, Physical and Engineering Sciences*, 2014, 470(2168): 20130847.
22. Bayındır C. Early detection of rogue waves by the wavelet transforms. *Physics Letters A*, 2016, 380(1-2): 156-161.
23. Gibson R, Swan C. The evolution of large ocean waves: the role of local and rapid spectral changes. *Proceedings of the Royal Society A: Mathematical, Physical and Engineering Sciences*, 2007, 463(2077): 21-48.
24. Gramstad O, Trulsen K. Fourth-order coupled nonlinear Schrödinger equations for gravity waves on deep water. *Physics of Fluids*, 2011, 23(6).
25. Li J, Yang J, Liu S, et al. Wave groupiness analysis of the process of 2D freak wave generation in random wave trains. *Ocean Engineering*, 2015, 104: 480-488.
26. Cui C, Pan W. Experimental study on the wavelengths of two-dimensional and three-dimensional freak waves. *China Ocean Engineering*, 2023, 37(1): 154-164.
27. Tao A, Zheng J, Chen B, et al. Properties of Freak Waves induced by two kinds of nonlinear mechanisms. *Coastal Engineering Proceedings*, 2012 (33): 73-73.
28. Liu S, Waseda T, Yao J, et al. Statistical properties of surface gravity waves and freak wave occurrence in crossing sea states. *Physical Review Fluids*, 2022, 7(7): 074805.
29. McAllister M, Draycott S, Adcock T, et al. Laboratory recreation of the Draupner wave and the role of breaking in crossing seas. *Journal of Fluid Mechanics*, 2019, 860: 767-786.
30. Wang L, Li J, Liu S, et al. Statistics of long-crested extreme waves in single and mixed sea states. *Ocean Dynamics*, 2021, 71: 21-42.
31. Rodriguez G, Soares C, Pacheco M, et al. Wave height distribution in mixed sea states. *J. Offshore*

1 *Mech. Arct. Eng.*, 2002, 124(1): 34-40.

2 32. Arena F, Soares C. Nonlinear high wave groups in bimodal sea states. *Journal of Waterway, Port,*  
3 *Coastal, and Ocean Engineering*, 2009, 135(3): 69-79.

4 33. Gramstad O, Trulsen K. Can swell increase the number of freak waves in a wind sea? *Journal of*  
5 *Fluid Mechanics*, 2010, 650: 57-79.

6 34. Wang L, Ding K, Zhou B, et al. Quantitative prediction of the freak wave occurrence probability in  
7 co-propagating mixed waves. *Ocean Engineering*, 2023, 271: 113810.

8 35. Wang L, Ding K, Zhou B, et al. Nonlinear statistical characteristics of the multi-directional waves  
9 with equivalent energy. *Physics of Fluids*, 2023, 35(8).

10 36. Wang L, Li J, Liu S, et al. Experimental and numerical studies on the focused waves generated by  
11 double wave groups. *Frontiers in Energy Research*, 2020, 8: 133.

12 37. Wang L, Zhou B, Jin P, et al. Relation between occurrence probability of freak waves and  
13 kurtosis/skewness in unidirectional wave trains under single-peak spectra. *Ocean Engineering*, 2022,  
14 248: 110813.

15 38. Ducroz G, Abdolhpour M, Nelli F, et al. Predicting the occurrence of rogue waves in the  
16 presence of opposing currents with a high-order spectral method. *Physical Review Fluids*, 2021, 6(6):  
17 064803.

18 39. Ducroz G, Bonnefoy F, Le Touzé D, et al. A modified high-order spectral method for wavemaker  
19 modeling in a numerical wave tank. *European Journal of Mechanics-B/Fluids*, 2012, 34: 19-34.

20 40. Bonnefoy F, Ducroz G, Le Touzé D, et al. Time domain simulation of nonlinear water waves  
21 using spectral methods. *Advances in numerical simulation of nonlinear water waves*. 2010: 129-164.

22 41. Dommermuth G, Yue P. A high-order spectral method for the study of nonlinear gravity waves.  
23 *Journal of Fluid Mechanics*, 1987, 184: 267-288.

24 42. West B J, Brueckner K A, Janda R S, et al. A new numerical method for surface hydrodynamics.  
25 *Journal of Geophysical Research: Oceans*, 1987, 92(C11): 11803-11824.

26 43. Agnon Y, Bingham B. A non-periodic spectral method with application to nonlinear water waves.  
27 *European Journal of Mechanics-B/Fluids*, 1999, 18(3): 527-534.

28 44. Rodriguez G, Soares C, Pacheco M, et al. Wave height distribution in mixed sea states. *J. Offshore*  
29 *Mech. Arct. Eng.*, 2002, 124(1): 34-40.

30 45. Ning D, Liang C, Chen L, et al. Numerical investigation on the propagation and evolution of  
31 focused waves over a sloping bed. *Ocean Engineering*, 2022, 250: 111035.

32 46. Zhou B, Ding K, Huang J, et al. Influence of uniform currents on nonlinear characteristics of  
33 double-wave-group focusing. *Physics of Fluids*, 2024, 36(3).

34 47. Feng X, Taylor P, Dai S, et al. Experimental investigation of higher harmonic wave loads and  
35 moments on a vertical cylinder by a phase-manipulation method. *Coastal Engineering*, 2020, 160:  
36 103747.

37 48. Chen L, Zang J, Taylor P, et al. An experimental decomposition of nonlinear forces on a surface-  
38 piercing column: Stokes-type expansions of the force harmonics. *Journal of Fluid Mechanics*, 2018,  
39 848: 42-77.

40 49. Ma Y, Tai B, Dong G, et al. An experiment on reconstruction and analyses of in-situ measured freak  
41 waves. *Ocean Engineering*, 2022, 244: 110312.

42 50. Redor I, Barthélemy E, Michallet H, et al. Experimental evidence of a hydrodynamic soliton gas.  
43 *Physical Review Letters*, 2019, 122(21): 214502.

44 51. Zhang J, Benoit M, Ma Y. Equilibration process of out-of-equilibrium sea-states induced by strong

- 1 depth variation: Evolution of coastal wave spectrum and representative parameters. *Coastal*
- 2 *Engineering*, 2022, 174: 104099.